IEEE Transactions on Robotics and Automation, Vol. 10, No. 1, February 1994, pp. 23-33,

2-D Contact Detection and Localization Using Proprioceptive Information

Manfred Huber and Roderic A. Grupen

Abstract— **This paper employs proprioceptive information (joint angles and torques) to estimate properties of the contact between a planar robot and an unknown object without specifically requiring strategic manipulator motions. The algorithm presented tackles this task in two stages; a contact localization analysis is followed by a force domain contact detection analysis. In the former, the Cartesian endpoint velocities are used for each link to obtain an estimate of the location of a hypothetical contact point on the link surface. A second observer, based on the displacement between two consecutive postures of the manipulator, provides an estimate of the error associated with this location. This data is fused over time by tracking the contact location using a linear observer and results in a hypothetical contact location, an associated uncertainty region, and a surface normal estimate. The detection phase uses torque domain evidence and the location estimates to verify the existence of each of the contacts. This process allows the detection of one contact per link and provides estimates of contact location, velocity, surface normal, and contact force.**

Keywords— **Contact Detection , Contact Localization , Proprioception , Kalman Filter**

I. Introduction

Perception of various aspects of the environment is essential for any agent to operate successfully in the real world. In the case of manipulating objects with articulate hands, some of the most important information is the point of contact and the Cartesian force between an object in the environment and the manipulator. This data is required for such different actions as force control in a whole-arm manipulator [6], incremental grasp configuration in multi-fingered robot hands [7] or modeling of unknown objects [1]. While vision could be used to obtain part of this information, it can not provide force data and has problems with concave objects and occlusions, illustrating the necessity of tactile sensing as a different means of perception.

When humans try to pick up an object in the dark, they first explore the location and shape of the object with the tactile sensors of their hand in order to determine the best grasp. To facilitate a similar performance for dextrous robot manipulators, anthropomorphic fingers with sensors [3] and tactile sensor arrays (see e.g. [12, 8] for an overview) have been developed and used in different applications (e.g. [16, 4]). This approach, however, requires the distribution of many "taxels" all over the manipulator, leading to packaging problems and changes in the characteristics of the robot. This paper will therefore pursue a different path by using proprioceptive information.

This work was supported in part by NSF IRI-9116297, CDA-8922572 and IRI-9208920.

The authors are with the Laboratory for Perceptual Robotics, Department of Computer Science, University of Massachusetts, Amherst, MA 01003.

In humans the proprioceptive system provides internal information about stretch in the tendons, degree of muscle contraction, and joint range limits which is used to infer the location of the limb (see e.g. [17] for details about human proprioception). Similar kinds of information are available for robot manipulators in the form of joint angles, velocities and torques. As opposed to the method of [2] which uses this information to refine parameters in an approximately known world model, the approach of this paper estimates contact locations and is based on no *a priori* knowledge about the environment.

Different methods to determine a contact point by means of proprioceptive information have been proposed. While [6] shows a way to infer the location of a single contact from the torques in two joints, [15, 18] require full force information (i.e. three forces and three moments) for the same task in 3 dimensions. The reliance on precise readings from the force/torque sensors limits these techniques to static observations without movements. Because of this and the imprecise torque data available from current manipulators, the approach of [9, 10] first detects a contact by observing the torques and then initiates strategic posture changes to determine the contact location via posture intersection. These "self posture changing motions" (spcm), however, allow only for the detection of the most distal contact on the manipulator and require specific finger movements. Another shortcoming is that no contacts on the fingertip can be found using this method. The algorithm proposed here tries to overcome these limitations while localizing 3D geometry within the medial plane of the finger. It employs the current motion of the finger, imposed by other task achieving behaviors, and three different observers based on geometric contact constraints and torque domain evidence to estimate the location and determine the existence of a contact for each link.

In the remainder of this paper, Section II introduces the constraints used in the algorithm while Section III discusses issues related to the modeling of uncertainties. Section IV finally presents some results of this approach in a geometric modeling task.

II. Contact Constraints

The algorithm presented in this paper tries to use rigid body constraints and violations of the equations of freespace dynamics to hypothesize the existence and location of contact points between a planar robot arm with revolute joints and parallel link surfaces and an unknown object. The object is assumed to be stationary and rigid and the robot provides the necessary information in the form of joint angles θ_i, joint velocities $\dot{\theta}_i$ and torques τ_i.

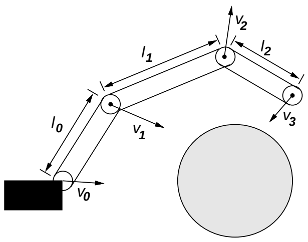

Fig. 1. Planar Robot Arm with Spherical Object

Figure 1 shows a three link manipulator of this type and some of the variables used throughout this paper, the most important of which are

θ_i^t	Joint angle
$\dot{\theta}_i^t$	Rotational velocity
τ_i^t	Joint torque
l_i	Link length
r_i	Half the width of the link
v_i^t	Cartesian velocity of joint axis
$p_i^t = \begin{pmatrix} x_i^t \\ y_i^t \end{pmatrix}$	Cartesian location of joint axis
P^t	Link Posture ,

where subscript i indicates the link/joint number and superscript t the time of the observation[1].

For the following geometric analysis, the parallel link surfaces and spherical tip regions are treated separately due to the differences in surface geometry.

A. Link Contacts

The location of a contact on link i is specified by the distance, d_i, from the proximal joint of this link and the side, s, of the link, which can be found based on the static torques and is represented as 1 or -1 for the left or right side of the link, respectively (The calculation of s is given in Equation 16).

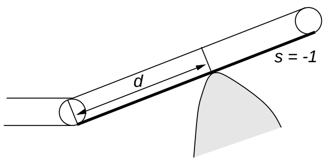

Fig. 2. Link Contact Coordinates

1) Posture Intersection: Kaneko and Tanie [10] use the intersection of two consecutive link postures as an approximation of the contact location. Similarly, this approach employs a corrected form of the intersection of the link axis as a first contact observation.

Using the properties in Figure 3, equations for an intersection point ξ of two link postures are given as

$$\xi = p_1^t + k^t \frac{1}{l} \begin{pmatrix} \ell_x^t \\ \ell_y^t \end{pmatrix}$$

[1] Subscripts and superscripts are avoided wherever possible to simplify the corresponding equations.

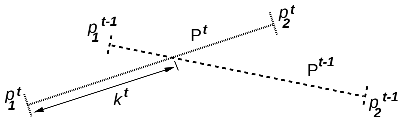

Fig. 3. Postures at Time $t-1$ and t

$$\left(\xi - p_1^{t-1}\right)^T \frac{1}{l} \begin{pmatrix} -\ell_y^{t-1} \\ \ell_x^{t-1} \end{pmatrix} = 0 \quad ,$$

where $\ell_x^t = x_2^t - x_1^t$.

From this, the intersection, k, in link coordinates can be derived as

$$k^t = l \frac{\Delta y_1 {\ell_x}^{t-1} - \Delta x_1 {\ell_y}^{t-1}}{{\ell_x}^t {\ell_y}^{t-1} - {\ell_y}^t {\ell_x}^{t-1}} \quad , \tag{1}$$

with $\Delta x = x^t - x^{t-1}$.

This location is not the precise position of the contact point but only an approximation which depends on the object curvature and the angle between the two postures. Therefore a compensation term is needed to correct this estimate.

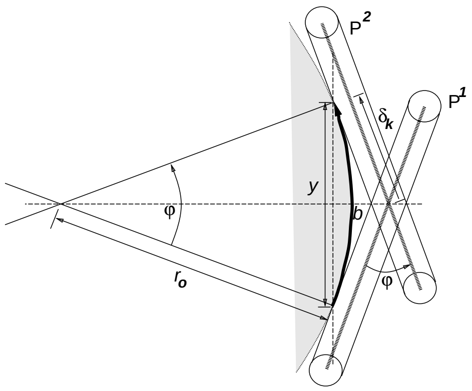

Fig. 4. Correction of Intersection Point

Assuming constant curvature of the object between two consecutive posture recordings, the situation illustrated in Figure 4 leads to

$$\begin{aligned} b &= r_o \varphi \quad (= \text{arc length}) \\ y &= 2(r_o + r) \sin \tfrac{\varphi}{2} \\ \delta_k &= \tfrac{y}{2} \tfrac{1}{\cos \frac{\varphi}{2}} \end{aligned}$$

and thus to a correction term, δ_k, of

$$\delta_k = \left(\frac{b}{\varphi} + r\right) \tan \frac{\varphi}{2} \quad , \tag{2}$$

where b is the contact displacement on the object surface.

Equations 1 and 2 provide then the corrected estimate of the contact, d',

$$d' = k + \delta_k \quad . \tag{3}$$

The only unknown remaining is b which is equivalent to the contact displacement $d^t - d^{t-1}$ on the link minus the distance the link slipped on the object.

2) Instantaneous Center of Velocity: Reuleaux [14] noted in 1875 that any planar motion of a lamina (or planar rigid body) is equivalent to a pure rotation about an instantaneous center. For a link of the manipulator, this point can be constructed as the intersection of the normals of the velocity vectors in the link endpoints as illustrated in Figure 5.

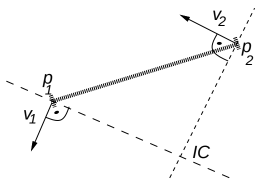

Fig. 5. Instant Center for one Link

In the case of a rolling contact without slip, the contact point coincides with the instantaneous center since the link pivots around it. In most situations, however, slip occurs, displacing the center from the link surface. Therefore the slip velocity, which is always tangential to the link surface, has to be compensated for in order to find the point of contact.

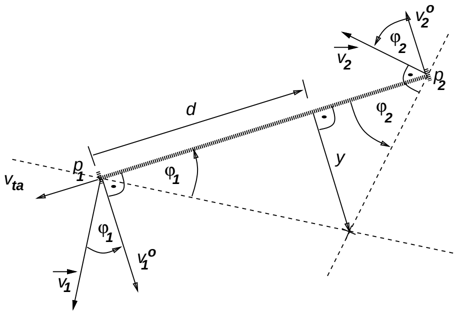

Fig. 6. Instant Center for Contact with Slip

In the following analysis, $\hat{\ell}$ and $\hat{n}$ denote the unit row vectors along and orthogonal to the link axis, respectively.

$$\begin{aligned}\hat{\ell} &= \tfrac{1}{l}\,(\ell_x,\ \ell_y) = \tfrac{1}{l}(p_2 - p_1)^T \\ \hat{n} &= \tfrac{1}{l}\,(-\ell_y,\ \ell_x)\ \ .\end{aligned}$$

Using the geometric properties illustrated in Figure 6, the following system of equations can be derived

$$\begin{aligned}\tan(\varphi_1) &= \tfrac{v_{ta}}{v_1^o} \\ \tan(\varphi_2) &= -\tfrac{v_{ta}}{v_2^o} \\ \tan(\varphi_1) &= -\tfrac{y}{d} \\ \tan(\varphi_2) &= -\tfrac{y}{l-d}\ \ ,\end{aligned}$$

which result in the terms

$$\begin{aligned}d &= l\tfrac{v_1^o}{v_1^o - v_2^o} \\ y &= l\tfrac{v_{ta}}{v_2^o - v_1^o}\end{aligned} \qquad (4)$$

for the location of the instantaneous center, where $v_i^o = \hat{n}\cdot v_i$ and $v_{ta} = \hat{\ell}\cdot v_1$.

In addition to establishing a contact location hypothesis, these equations also estimate the slip velocity, v_{ta}, since for link i, $v_2^o - v_1^o = l\sum_{j=0}^{i}\dot{\theta}_j$.

B. Tip Contacts

As for the link, the contact location on the spherical fingertip and knuckle regions can be found by means of relations between manipulator motions and contact constraints. In order to specify these relations, tip contacts are represented as the angle ϕ of the surface normal of the object with respect to the body centered coordinate frame.

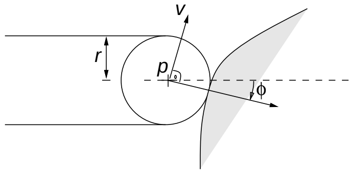

Fig. 7. Tip Contact Representation

1) Velocity-Location Relation: In the presence of a tip contact, the Cartesian velocity vector of the center of the tip is always tangential to the surface of the object at the point of contact. As shown in Figure 7, this determines the contact location ϕ relative to the x-direction as

$$\left(\begin{array}{c}\cos\phi\\ \sin\phi\end{array}\right) = \pm\frac{1}{\|v\|}\left(\begin{array}{c}-v_y\\ v_x\end{array}\right)\ , \qquad (5)$$

which yields a unique solution since the touchable part of the tip is only a hemisphere.

2) Displacement-Location Relation: In the same way as the endpoint velocity, the displacement $\Delta p = (\Delta x, \Delta y)^T$ between two consecutive postures can be used to obtain an estimate ψ of the contact location, where

$$\left(\begin{array}{c}\cos\psi\\ \sin\psi\end{array}\right) = \pm\frac{1}{\|\Delta p\|}\left(\begin{array}{c}-\Delta y\\ \Delta x\end{array}\right)\ . \qquad (6)$$

To correct for the curvature dependent error in this approximation, a correction term δ_ψ is required. Assuming constant curvature of the object between two consecutive contact estimations, this term can be derived from the geometric relations shown in Figure 8.

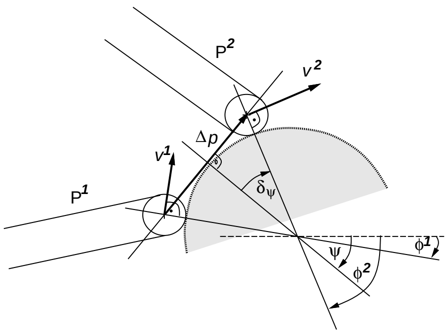

Fig. 8. Correction for Displacement Based Point

Using these properties, δ_ψ is given by

$$\delta_\psi = \frac{1}{2}\left(\phi^2 - \phi^1\right)\ \ , \qquad (7)$$

thus resulting in a corrected angular representation for the contact of

$$\phi' = \psi + \delta_\psi\ \ . \qquad (8)$$

III. The Algorithm

The algorithm proposed here combines the constraints described in the previous section with additional torque information to determine the points of contact in three stages:

A. Possible contact positions and normals for each link are estimated by means of position and velocity evidence, based on the assumption that contact exists.
B. Constraints on the position and velocity of contact points are used to decide whether a link or tip contact is more probable.
C. Torque domain evidence is utilized to verify the existence of a contact point and to estimate the corresponding contact force.

In order to do this reliably, uncertainties have to be taken into account in all three steps.

A. Contact Localization

Geometric relations like those described in Section II only yield exact results if all the variables are precisely known. In a robot environment, however, sensor readings are imprecise, objects are not perfectly rigid and other kinds of noise exist. To cope with the arising uncertainties, the contact point is tracked over the link surface, incrementally including new estimates using a discrete Kalman filter (see e.g. [5]). All links are thereby strictly independent i.e. no observations on one link influence any other link.

1) Link Contacts: Because of the known kinematics of the manipulator, Equation 4 provides an estimate of the slip velocity of the link on the object and a hypothesis of the contact location. Using the latter as the measurement in the system description

$$\begin{array}{ll} \bar{d}^t = \bar{d}^{t-1} + v_c \Delta t + \varrho^{t-1} & \text{as a system model} \\ d = d_c + \rho^{t-1} & \text{for the new measurement} \quad , \end{array}$$

where

$$\begin{array}{ll} \bar{d}^t & = \text{Contact location at time } t \\ v_c & = \text{Contact velocity on the link surface} \\ \varrho^t & = \text{Noise process described by } N\left(0, \sigma_\varrho^2(t)\right) \\ d_c & = \text{Actual contact position} \\ \rho^t & = \text{Noise process described by } N\left(0, \sigma_\rho^2(t)\right) \quad , \end{array}$$

allows the combination of old and new evidence to a more precise location $\hat{d}$ and a qualitative estimate of the associated uncertainty by means of a linear Kalman filter.

Since the variances $\sigma_\varrho^2(t)$ and $\sigma_\rho^2(t)$ are not known, they are replaced by error bound estimates $\varepsilon_{v_c}\Delta t$ and ε_d for the prediction and measurement, respectively. Using this, the estimator equations can be derived as:

$$\begin{array}{l} \hat{d}^t = \left(\hat{d}^{t-1} + v_c \Delta t\right) + K^t \left(d - \left(\hat{d}^{t-1} + v_c \Delta t\right)\right) \\ \hat{\varepsilon}^t = \varepsilon_d K^t \\ K^t = \frac{\hat{\varepsilon}^{t-1} + \varepsilon_{v_c}\Delta t}{\varepsilon_d + \hat{\varepsilon}^{t-1} + \varepsilon_{v_c}\Delta t} \quad , \end{array} \tag{9}$$

with

$$\begin{array}{ll} \hat{d}^t & = \text{Filtered location at time } t \\ d & = \text{Location hypothesis of Equation 4} \\ v_c & = \text{Estimated contact point velocity} \\ \hat{\varepsilon}^t & = \text{Uncertainty associated with } \hat{d}^t \\ \varepsilon_d & = \text{Uncertainty associated with } d \\ \varepsilon_{v_c} & = \text{Uncertainty associated with } v_c \quad . \end{array}$$

In order to use this observer, however, values for the unknown variables v_c, ε_{v_c} and ε_d have to be found. For the first two, a filtered version of $\frac{\Delta \hat{d}}{\Delta t}$ and $\frac{\hat{\varepsilon}^t + \hat{\varepsilon}^{t-1}}{\Delta t}$ can be used as an approximation of the actual contact velocity on the link and the corresponding uncertainty. The derivation of an estimate for the latter, using the intersection hypothesis d' as a second observation, is shown in the next section.

2) Uncertainty Propagation for Link Contacts: The correction term of Equation 2 contains, besides the angular displacement $\varphi = \sum \Delta\theta_j$, the distance b that the contact traveled on the object surface. An estimate for this term can be found from the relation

$$(b + d_s) \cong \left(d - \hat{d}^{t-1}\right) \quad ,$$

where, assuming a constant slip acceleration between two observations,

$$\begin{array}{ll} b & = \text{Distance due to rolling} \\ d_s \approx \frac{v_s^t + v_s^{t-1}}{2}\Delta t & = \text{Distance due to slip} \\ v_s^t & = \text{Slip velocity} \\ d & = \text{Instant center observation} \\ \hat{d}^{t-1} & = \text{Last estimate} \quad . \end{array}$$

Taking this estimate for b and the intersection point k, the intersection hypothesis d' can be derived as a second observation, based on the correctness of the variables used. In reality, however, the current observation and the previous estimate may both have associated errors in the range of $\pm\varepsilon_d$ and $\pm\hat{\varepsilon}^{t-1}$, respectively. Since an error estimate for the previous estimate is given *a priori* by the filter in Equation 9 , the worst case error in the new observation can be found using Equations 2 and 3 by assuming that the actual location of the contact $d_c = d \pm \varepsilon_d$. This leads to

$$d_c - k = \left(\frac{d \pm \varepsilon_d - \hat{d}^{t-1} \pm \hat{\varepsilon}^{t-1} - d_s}{\varphi} + r\right) \tan\frac{\varphi}{2} \quad ,$$

which can be transformed into

$$\pm\varepsilon_d = \frac{\pm\hat{\varepsilon}^{t-1}\frac{1}{\varphi}\tan\frac{\varphi}{2} + d' - d}{1 - \frac{1}{\varphi}\tan\frac{\varphi}{2}}$$

and results in an expression for the error bound in the contact location estimate of

$$\varepsilon_d \leq \frac{\hat{\varepsilon}^{t-1}\frac{1}{\varphi}\tan\frac{\varphi}{2} + \left|d' - d\right|}{1 - \frac{1}{\varphi}\tan\frac{\varphi}{2}} \qquad \text{for } \frac{\tan\frac{\varphi}{2}}{\varphi} < 1 \quad . \tag{10}$$

This term can then be used in Equation 9 to compute the contact location.

3) Tip Contacts: Similar to the case of the link, the behavior of a tip contact can be expressed using the linear equations

$$
\begin{array}{ll}
\bar{\phi}^t = \bar{\phi}^{t-1} + \omega \Delta t + \varrho^{t-1} & \text{for the system} \\
\phi = \phi_c + \rho^{t-1} & \text{as a measurement model} \quad ,
\end{array}
$$

with

$$
\begin{array}{ll}
\bar{\phi}^t & = \text{Contact location at time } t \\
\omega & = \text{Angular contact point velocity} \\
\varrho^t & = \text{Noise process described by } N\left(0, \sigma_\varrho^2(t)\right) \\
\phi_c & = \text{Actual contact position} \\
\rho^t & = \text{Noise process described by } N\left(0, \sigma_\rho^2(t)\right) \ .
\end{array}
$$

Replacing the variances again with error estimates results in a location estimate $\hat{\phi}$ and an estimate of the corresponding angular uncertainty. The equations for this filter are nearly identical to those used for the link.

$$
\begin{array}{l}
\hat{\phi}^t = \left(\hat{\phi}^{t-1} + \omega \Delta t\right) + K^t \left(\phi - \left(\hat{\phi}^{t-1} + \omega \Delta t\right)\right) \\
\hat{\epsilon}^t = \epsilon_\phi K^t \\
K^t = \frac{\hat{\epsilon}^{t-1} + \epsilon_\omega \Delta t}{\epsilon_\phi + \hat{\epsilon}^{t-1} + \epsilon_\omega \Delta t} \quad ,
\end{array}
\tag{11}
$$

where

$$
\begin{array}{ll}
\hat{\phi}^t & = \text{Filtered location at time } t \\
\phi & = \text{Location hypothesis of Equation 5} \\
\omega & = \text{Angular contact point velocity} \\
\hat{\epsilon}^t & = \text{Uncertainty associated with } \hat{\phi}^t \\
\epsilon_\phi & = \text{Uncertainty associated with } \phi \\
\epsilon_\omega & = \text{Uncertainty associated with } \omega
\end{array}
$$

The variables ω and ϵ_ω are similarly given by $\frac{\Delta \hat{\phi}}{\Delta t}$ and $\frac{\hat{\epsilon}^t + \hat{\epsilon}^{t-1}}{\Delta t}$. To determine the remaining unknown ϵ_ϕ, the displacement based hypothesis $\phi^{'}$ of Equation 8 is employed, using ϕ and $\hat{\phi}^{t-1}$ as the contact locations for the two postures. As in the case of the link, this leads to an error analysis using Equation 7 and 8 described in the next section.

4) Uncertainty Propagation for Tip Contacts: Making the same assumptions as in the case of link contacts, and setting the correct contact location to $\phi_c = \phi \pm \epsilon_\phi$ yields

$$
\phi_c - \psi = \frac{1}{2}\left(\phi \pm \epsilon_\phi - \hat{\phi}^{t-1} \pm \hat{\epsilon}^{t-1}\right) \ ,
$$

which leads to

$$
\pm \epsilon_\phi = \pm \hat{\epsilon}^{t-1} + 2\left(\phi^{'} - \phi\right)
$$

and finally provides a worst case error which can be used in the filter of Equation 11.

$$
\epsilon_\phi \leq \hat{\epsilon}^{t-1} + 2\left|\phi^{'} - \phi\right| \tag{12}
$$

B. Link/Tip Decision

Since tip and link are treated separately, the localization phase results in a possible contact location for the link and for the tip which are maximally consistent with the respective constraints. In most cases, however, only one contact with the object exists, requiring a decision for one of the two hypotheses. In order to do this, a heuristic based on additional constraints on the location and the motion of the contact point is used [2].

1) Impossible Location of Link Contact: Since the contact estimate is based on the instantaneous center of rotation, many situations with a tip contact result in an impossible hypothesis (i.e. $\hat{d} < 0 \ \vee \ \hat{d} > l$). Taking the uncertainty associated with the location into consideration, this can be transformed into a measure of evidence $E_{\hat{d}}^-$ against a link contact, where

$$
E_{\hat{d}}^- = \begin{cases} \frac{\hat{d} - l}{\hat{\varepsilon}} & \text{for } \hat{d} > l \\ \frac{-\hat{d}}{\hat{\varepsilon}} & \text{for } \hat{d} < 0 \\ 0 & \text{otherwise} \ . \end{cases} \tag{13}
$$

2) Impossible Motion of Link Contact: A second constraint for the link contact is given by its motion. In the absence of slip, the rotational direction of the link around the contact point determines whether the contact moves up or down this link as shown in Figure 9.

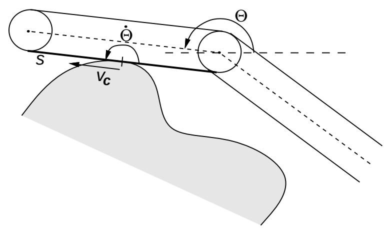

Fig. 9. Contact Point Velocity without Slip

Including slip and relating this to the uncertainty involved in the contact velocity results in a second counterevidence measure $E_{v_c}^-$ with

$$
E_{v_c}^- = \frac{\max\left(0, \ -s \cdot sign\left(\dot{\Theta}\right)(v_c - v_s)\right)}{\varepsilon_{v_c}} \quad , \tag{14}
$$

where

$$
\begin{array}{ll}
v_c & = \text{Contact velocity of Equation 9} \\
v_s & = \text{Slip velocity} \\
s & = \text{Contact side of the link} \\
\dot{\Theta}_i = \left(\sum_{j=0}^{i} \dot{\theta}_j\right) & = \text{Rotational velocity for link } i \ .
\end{array}
$$

3) Impossible Location of Tip Contact: In a similar way, a restriction for possible tip contact locations exists. Since the side, s, for the link position is based on torque evidence, it limits contacts to one side of the link. Using this, the

[2]This can not succeed in general because of the possibility of having simultaneous contacts on concave objects. The motions in these cases can produce the same sensory signature as either of the equivalent single contact cases, leading necessarily to a wrong decision.

location $\hat{\phi}$ of the contact can be tested and evidence, $E^-_{\hat{\phi}}$, against the existence of the hypothesized tip contact, can be found as

$$E^-_{\hat{\phi}} = \frac{\max\left(0,\ -s\left(\hat{\phi} - \Theta\right)\right)}{\hat{\epsilon}} \quad , \tag{15}$$

where

$$\begin{array}{l} \Theta_i = \sum_{j=0}^{i} \theta_j = \text{Angular orientation of link } i \\ \left(\hat{\phi} - \Theta\right) \text{ scaled between } -\pi \text{ and } \pi \quad . \end{array}$$

These three sources of evidence, expressed by Equations 13, 14 and 15 can then be combined in a heuristic to form the decision for either the link or tip contact, resulting in a single contact hypothesis per link [3].

C. *Contact Detection*

While all the kinematic constraints used so far give a hypothesis of the possible location of a contact, they can not determine its existence. The reason for this is that the criteria in the localization stage are purely based on the motion of the finger which can always be "simulated" in the absence of an interaction with the environment. To resolve this ambiguity, additional information has to be used. The approach taken here employs the joint torques τ as a third observation, which also provides the side, s, used in the previous sections.

1) Torque Decomposition: Since any interaction between an object and the manipulator results in a force, and thus torques in the joints, each contact with an object leads to a violation of the equations of freespace dynamics of the robot. A single contact produces thereby a unique set of joint torques but since it causes torques in all proximal joints, this information becomes ambiguous in the presence of multiple contact points. Given the location and surface normal for the most distal contact, however, and assuming that no friction and dynamic effects are present, the existence of this contact and its interaction force can be determined using only the torque in the proximal joint of the corresponding link. From this, the side, s, can be found as

$$s = sign\left(\tau\right) \tag{16}$$

because of the relation between contact force and torque in this joint. To derive the magnitude of the force for a frictionless contact, the additional considerations illustrated in Figure 10 are necessary.

Using the variables shown in this construction, relations

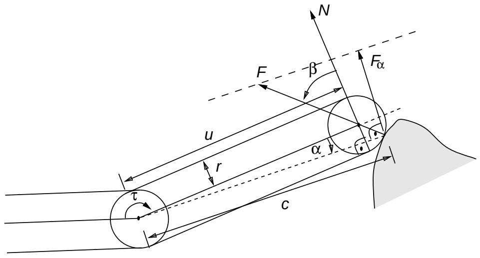

Fig. 10. Contact Force Construction

between the different properties arise as

$$\begin{array}{ll} c & = \sqrt{\left(u + r\sin\beta\right)^2 + \left(r\cos\beta\right)^2} \\ \begin{pmatrix} \sin\alpha \\ \cos\alpha \end{pmatrix} & = \frac{1}{c}\begin{pmatrix} r\cos\beta \\ u + r\sin\beta \end{pmatrix} \\ \left|F_\alpha\right| & = \frac{|\tau|}{c} \quad , \end{array}$$

leading to a contact force F of

$$|F| = \frac{|F_\alpha|}{\cos\left(\alpha + \beta\right)} = \frac{|\tau|}{c \cdot \cos\left(\alpha + \beta\right)} \tag{17}$$

for a point contact without friction[4], where

$$\left.\begin{array}{ll} u & = \hat{d} \\ \beta & = \left(s + 1\right)\frac{\pi}{2} \end{array}\right\} \text{ for link contacts}$$
$$\left.\begin{array}{ll} u & = l \\ \beta & = \frac{\pi}{2} + \hat{\phi} - \sum_{j=0}^{i} \theta_j \end{array}\right\} \text{ for tip contacts} \quad .$$

This calculation is possible because the direction of the force coincides with the surface normal of the object at the contact point (which is identical to the normal of the link surface at this location), and determines the torques induced in all the joints proximal to the corresponding link i via the relation

$$\vec{\tau} = J_i^T F \quad , \tag{18}$$

where J_i is a partial Jacobian of the manipulator using $l_i = c$, $\theta_i = \theta_i + \alpha$ and $l_j = 0$ for $j > i$.

Subtracting these values from the initial torque measurements results in the set of torques caused by more proximal contacts and thus permits a recursive decomposition into individual contact components.

2) Incorporation of Uncertainties: Due to the dynamics involved in manipulator motions, the measured torques are different from the ones caused by external forces. To be able to do the decomposition under these circumstances, it is therefore necessary to compensate for the robot dynamics, requiring a model of the freespace dynamics. Since such a model is in most cases not perfect, an upper and a lower bound are used here to perform a worst case analysis of the torque data [5].

In the same way as the extreme cases of the manipulator dynamics, the uncertainties in the location of the link

[3]The term used for the experiments in Section IV, for example, is the simple linear combination

$$sign\left(0.5 + E^-_{\hat{\phi}} - E^-_{\hat{d}} - E^-_{v_c}\right) \quad ,$$

where 1 denotes link and -1 tip contact.

[4]This equation could be simplified to $F = \frac{|\tau|}{u\cos\beta}$. This simpler formulation, however, does not allow for an easy incorporation of Coulomb friction.

[5]An accurate model is not required in most cases since the contact localization can be expected to occur during low velocity movements and therefore only needs good inertial parameters.

contact $\pm\hat{\varepsilon}$ and in the direction of the force $\pm\hat{\epsilon}$ for tip contacts allow for variations in the contact force and thereby in the resulting torques. In order to detect a contact it is therefore necessary to determine if the measured torque is outside the "torque interval" created by all the uncertainties in the dynamics and distal contacts. Because the function for torques in the proximal joints is monotonic in the location u and the angle β of the contact force[6], the range of torques caused by the current contact can be found from Equations 17 and 18 by considering all combinations of the extreme location values u and β.

Using this approach, all location uncertainties of the previous sections can be integrated, allowing for a decision based on the whole uncertainty interval for each contact point and the dynamics of the robot. As a result of this exponential process, possible ranges of contact forces can be associated with each contact point.

3) Friction: All considerations so far have been based on the assumption of the absence of friction. To overcome this limitation, a way to incorporate Coulomb friction into the algorithm is presented in this section.

Coulomb friction can be seen as a pure uncertainty in the direction of the contact force, represented by the friction cone, and does therefore not interfere in any way with the kinematic constraints used in the localization stage. The only changes required are in the detection phase, where the uncertainty in the force direction has to be integrated into the worst case torques. This, however, can easily be done by adapting Equation 17 to

$$|F| = \frac{|\tau|}{c \cdot \cos(\alpha + \beta \pm \vartheta)} \ , \qquad (19)$$

where

$$\begin{gathered} \tan\vartheta = \mu_f = \text{maximum coefficient of friction} \\ (\alpha+\beta+\gamma) \in \left(\ (2k-1)\,\tfrac{\pi}{2}, (2k+1)\,\tfrac{\pi}{2}\ \right). \end{gathered}$$

Using this in the calculations of Section III.C.2 provides a worst case analysis that includes Coulomb friction.

IV. Experiments

A. Simulation Results

The performance results presented in this section were obtained from a dynamic robot simulator, modeling the object surface as a damped spring. The objects are therefore elastic and introduce uncertainty into the analysis. For the algorithm, the error estimates of Equations 10 and 12 are used in the filter equations 9 and 11, respectively, and the simple heuristic, $sign(0.5 + E^-_{\hat{\phi}} - E^-_{\hat{d}} - E^-_{v_c})$, with 1 denoting link and -1 tip contact, is employed for the link/tip decision process. The simulated manipulator has links of length $0.22225m$, $0.15875m$, and $0.127m$ respectively and achieves compliance by means of a PD controller, regulating the finger's position relative to reference angles $\theta_{ref_i} = \pi/4$. Throughout each experiment the manipulator's coordinate frame is moved with a constant velocity ($0.33m/s$) in the negative x-direction. To illustrate the performance of the algorithm, both smoothly curved and polygonal objects are presented and the data is discussed.

Figure 11 shows a sequence of snapshots of the robot interacting with a circular object and the data obtained during this movement. The radii of the circles representing the contact estimates denote the associated uncertainty obtained by the Kalman filter of the localization part. The statistics on the right show probability distributions for the absolute distance between the object surface and the hypothesized contact points, with outliers denoting all points with an error of more than $2mm$.

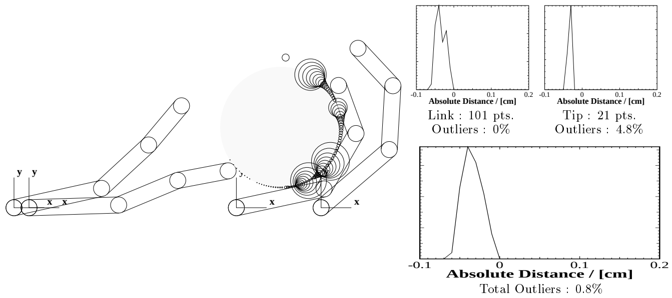

Fig. 11. Absolute Distance Error for Spherical Object

During this experiment multiple contacts on the manipulator occur, leading to up to 3 simultaneous contact observations. The data resulting from this shows only one tip contact point outside the object while all the other estimates are up to $0.6mm$ inside (recall that this is an elastic object and that the manipulator must push on it in order to observe it). The obvious outlier directly above the object is due to an incorrect decision for the tip instead of the link during the initial contact.

In the same way as above, a concave polygon is presented in Figure 12 as a second object.

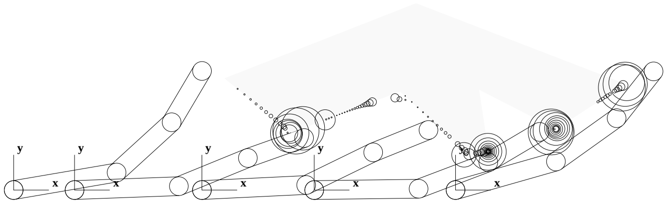

Fig. 12. Contacts for Concave Object

In this case, additional problems are caused by the sudden changes between different contacts on a single link in the vicinity of corners. Under these circumstances, the contact point is not moving continuously over the link surface and thus some assumptions for the filter are violated. The effects of this are the high uncertainties associated with the first link contacts for each corner. Similarly, line contacts between the link surface and a face of the polygon result in an ambiguous situation for the algorithm and might cause a wrong contact hypothesis. A third source of error is the loss of contact at the concavities which introduces additional dynamic effects in the manipulator. Because of all these difficulties, worse results can be expected here.

[6] A proof for this is given in the Appendix.

Figure 13 shows statistics of the absolute error and the one related to the error estimate for this object. Outliers in these two graphs denote all points with an error greater than $4mm$ or the error estimate, respectively.

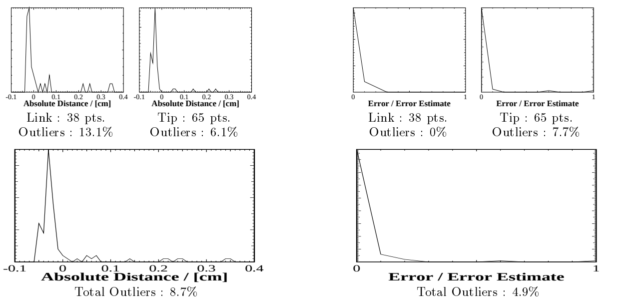

Fig. 13. Absolute and Relative Distance Error for Concave Object

As predicted, a higher number of outliers can be found here, leaving still 91.3% of all points within a range of $4mm$ (85.5% in $2mm$) and 95.1% within their associated error estimates.

These results show that the approach presented here expands to different object shapes although they do not fulfill all the assumptions used for the geometric analysis.

B. Robot Experiments

The results shown in this section were obtained using the index finger of a Utah/MIT dextrous robot hand mounted on a GE P50 robot. Similar to the simulations presented in the previous section, a geometric modeling task is performed using the P50 manipulator to move the hand along a straight line trajectory while compliance of the finger is established by a PD controller, employing constant reference angles θ_{ref}. The objects are fixed to the table to avoid slippage caused by the interaction forces with the finger.

Before performing these experiments, however, the algorithm has to be adapted to the characteristics of this setup. These changes are presented in the following section before Sections IV.B.2 and IV.B.3 show results obtained with different objects and discuss this data.

1) Algorithmic Setup: The location estimates of the approach presented in the preceding sections is based on geometric constraints of a contact between the manipulator and the object and relies therefore on knowledge of the arm geometry. A first step to adjust the algorithm to the new manipulator is therefore the incorporation of conical link regions[7]. As illustrated in Figure 14, this can be accomplished by modeling each link surface as the surface of a rectangle, reducing the problem to the simple computation of new endpoint locations and velocities for this altered geometry. This solution is also supported by the fact that the contact side and therefore the corresponding "rectangular link" can be determined before the geometric contact localization, thus leaving the rest of the localization phase unchanged.

In the detection phase, the required joint torques are

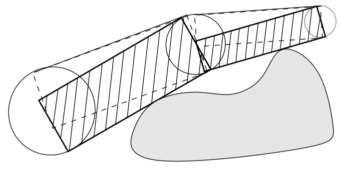

Fig. 14. Treatment of Conical Links

computed from the tendon tensions by means of a decoupling matrix (see [11] for detail). The resulting values for the circular peg example of Figure 16 are shown in Figure 15.

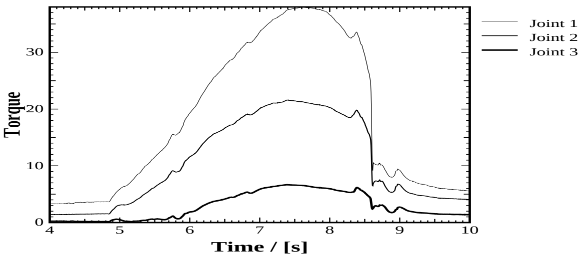

Fig. 15. Torque Data

This figure shows also the influence of friction in the joints and pulleys on the torque measures. Even after the finger looses contact with the object, these values stay far above 0, which has to be integrated into the dynamic analysis. For the initial experiments presented here, a simple constant upper and lower threshold was used as a dynamic model, representing mainly the internal friction and damping of the finger which dominate all other dynamic effects at the rather low speeds ($\approx 4cm/s$) used for these examples.

2) Results: For the following experiments, the raw input data, in form of angles and velocities, was recorded at a rate of $200Hz$ and then smoothed, using the running average over 5 values. These smoothed values were then used as input for the localization algorithm which was performing observations at a frequency of $50Hz$.

Figure 16 shows a sequence of snapshots of the finger interacting with a cylindrical peg, taken from an overhead camera. The black circles in the right picture show the contact estimates projected onto the image, where the radii represent the associated uncertainty determined by the Kalman filter. Only points with uncertainties below a threshold of $1.0cm$ are used.

The raw data produced by the algorithm for this example is shown in Figure 17. The left picture represents thereby the shape reconstructed by simple connection of the estimated contact points regardless of their individual uncertainties. In a similar way, the right plot shows the local normal vectors computed for each of these points.

In the same way as for the round peg, Figure 18 shows a series of snapshots taken during an analogous experiment with a rectangular peg.

The two pictures in Figure 19 show the shape reconstructed by simple straight line connection of the location

[7] Inconsistencies with this model in the joint regions of the Utah/MIT hand are omitted.

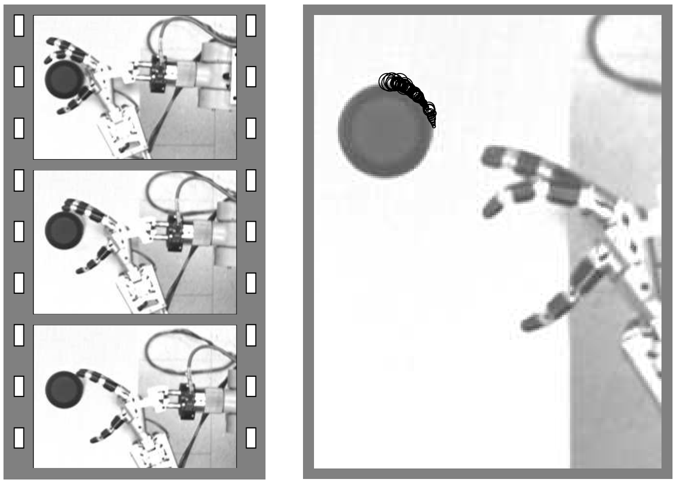

Fig. 16. Utah/MIT Hand with Circular Object

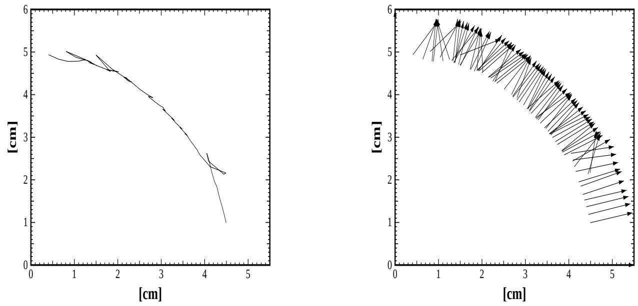

Fig. 17. Shape and Normal Estimates for Circular Object

estimates and the hypothesized surface normals in these points, respectively.

In this example, the points and normals on the top face of the rectangle show rather high errors although all the normals are still within the predicted uncertainty interval. One of the reasons for this degraded performance can be seen in the readings of the joint angle sensors of the finger presented in Figure 20.

These graphs exhibit extensive, relatively low frequency

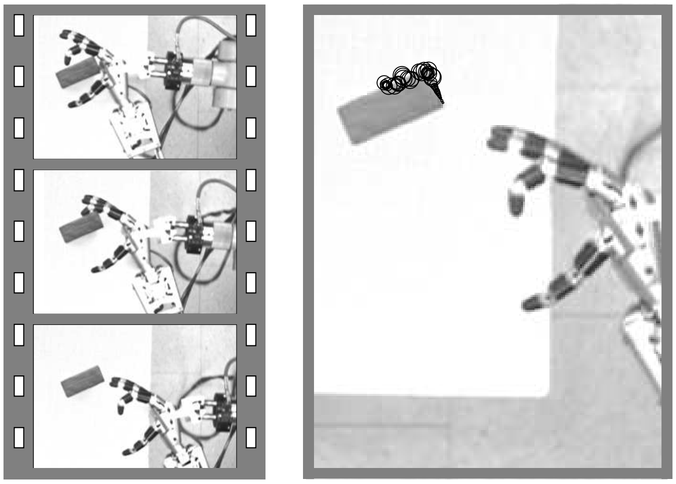

Fig. 18. Utah/MIT Hand with Rectangular Object

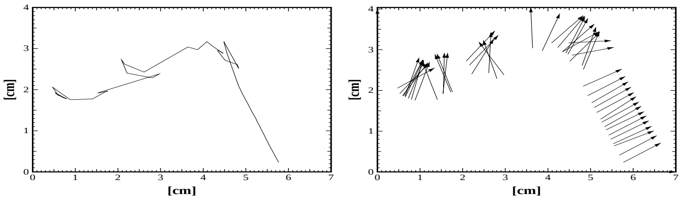

Fig. 19. Shape and Normal Estimates for Rectangular Object

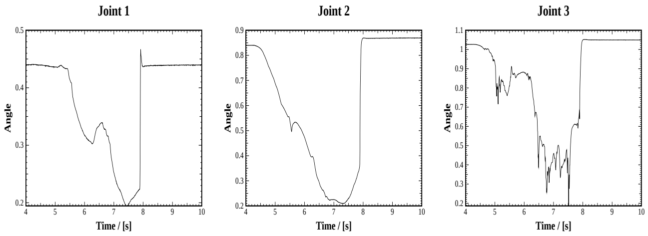

Fig. 20. Angle Sensor Readings for Rectangular Peg

noise in joint 3 which leads to imprecise location and velocity values in the geometric analysis. Because of the resulting inconsistent contact hypotheses, the algorithm reacts to this by increasing the uncertainty estimates for the points, thereby incorporating sensor noise without explicit modeling. Since some of the noise is probably a result of problems with the actuators and sensors of the hand, which appeared at the time the experiments were performed, better results than the ones presented should be possible.

A second problem appears as a direct result of the experimental setup. Since no force control was used for the finger and the P50 robot, the gains of the PD controller of the hand had to be chosen rather low to avoid high contact forces and thus movements of the object. This, however, decreases the signal to noise ratio for the torque signal and therefore the detectability of a contact. A better performance of the detection phase could therefore be achieved by means of a different controller for the robot and the finger.

In spite of all these problems, however, the results shown here still illustrate the applicability of this approach to a real robot.

3) Repeatability: Many applications require rather precise models of objects in the environment. In order to build these hapticly, contact observations have to be repeatable, thus allowing improved quality by observing one location multiple times.

To examine the repeatability for the algorithm presented in this paper, an additional experiment was conducted using the thumb of the robot hand. 20 sweeps over a circular peg were performed, moving the P50 robot by hand and thus producing different trajectories and contact forces for each one.

The connected contact estimates for all 20 sweeps are presented in Figure 21.

These lines show a maximum difference between the observations of approximately $5mm$. These discrepancies are mainly due to the errors propagating through the kinematics of the P50 and the finger, slight non-repeatable move-

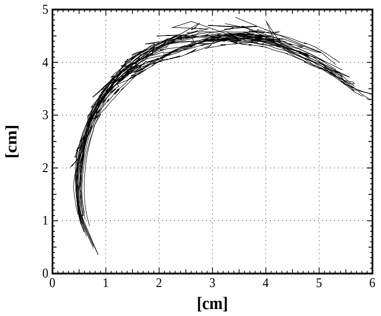

Fig. 21. 20 Sweeps over Circular Object

ments of the peg caused by varying contact forces, and contact localization errors. Considering all this, a repeatability error of $\pm 2mm$ demonstrates the applicability of this approach to model building and other tasks.

The major limiting factor for the precision of the observations is the quality of the forward kinematics and geometry for the system. If these are not exactly known, errors in the output occur. Circular fits to individual sweeps, like the one presented in Figure 22, exemplify this.

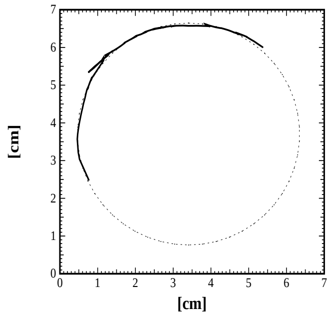

Fig. 22. Circular Fit to Contact Data

For the above experiment the radii of the least squared error circular fits for all the sweeps are between $2mm$ and $3mm$ too small and the contact estimates show a slightly elliptical shape due to small errors in the hand kinematics and the finger diameters. If these values are known precisely, even better performance of the algorithm can be expected.

V. Conclusions

The algorithm presented in this paper permits to collect contact information while interacting with an unknown object using only joint angle and torque sensors. In order to do this, it requires manipulator motion throughout the localization. For tasks like geometric modeling, where gathering data is the main objective, it is possible to execute specific movements to obtain the highest quality data. Such an active sensing strategy, however, may in different applications violate constraints imposed by other objectives of the manipulation task. For this reason, the approach used here employs arbitrary motions to derive information opportunistically during general interactions with the object.

Although the analysis is based on rigid objects and some additional assumptions, the experiments performed show that this approach is also able to handle objects which do not fulfill all these requirements. A second observation made is that although not explicitly modeled, noise in the sensors and the environment is incorporated into the uncertainty estimates of the algorithm by means of its effects on the geometric relations used.

As seen in Section IV.B.1, implementations of this algorithm on real robots require some of the equations to be changed to reflect the actual arm geometry. The influence of such a change, however, is limited to changes in the equations of Section II for the intersection and instantaneous center, leaving the underlying method unchanged.

To extend this approach to contacts outside the medial plane, additional information seems to be necessary since the intersection and instant center hypothesis both result in a curve rather than a point on the link surface. One possibility for this would be to allow only one contact on the whole manipulator to occur and then use the line of action of the force derived from the torques in all the joints as an additional location estimate. All this could then again be integrated using a Kalman filter approach for a two parameter contact location.

Appendix

Assuming a contact on link n at distance c with an angle towards the link normal of γ, the torque τ_m at link m caused by this contact is

$$\tau_m = |F|\, J_n^T \begin{pmatrix} -\sin\left(\Theta_0^n + \gamma\right) \\ \cos\left(\Theta_0^n + \gamma\right) \end{pmatrix} ,$$

where Θ_j^k denotes $\sum_{i=j}^{k} \theta_i$.

Using Equation 17 and the Jacobian leads then to

$$\tau_m = \frac{|\tau_n|}{c\cos\gamma} \sum_{j=m}^{n-1} \Big(l_j \sin\Theta_0^j \sin\left(\Theta_0^n + \gamma\right) + l_j \cos\Theta_0^j \cos\left(\Theta_0^n + \gamma\right) \Big) + \tau_n \quad ,$$

which simplifies to

$$\tau_m = \frac{|\tau_n|}{c} \sum_{j=m}^{n-1} \left(l_j \left(\cos\Theta_{j+1}^n - \sin\Theta_{j+1}^n \tan\gamma \right) \right) + \tau_n \quad .$$

Monotonicity in γ

To show the monotonicity of the torques in the direction γ of the force, τ_m has to be differentiated with respect to γ resulting in

$$\frac{\partial \tau_m}{\partial \gamma} = -\frac{|\tau_n|}{c} \sum_{j=m}^{n-1} \left(l_j \sin\Theta_{j+1}^n \right) \frac{1}{\cos^2\gamma} \quad ,$$

which is continuous for $\gamma \neq (2k+1)\frac{\pi}{2} \ : \ k \in Z$ and has no local maxima or minima. The torque τ_m is therefore monotonic in γ for $\gamma \in \left(\ (2k-1)\frac{\pi}{2}, (2k+1)\frac{\pi}{2}\ \right)$.

Monotonicity in c

In a similar way, the monotonicity in c can be shown by the following derivative

$$\frac{\partial \tau_m}{\partial c} = -\frac{|\tau_n|}{c^2} \sum_{j=m}^{n-1} \left(l_j \left(\cos \Theta_{j+1}^n \right) - \sin \Theta_{j+1}^n \tan \gamma \right) \quad ,$$

which is again continuous for $c \neq 0$ and without local extrema, meaning that τ_m is also monotonic in c for $c \in (-\infty, 0)$ or $c \in (0, \infty)$.

References

[1] P.K. Allen. Haptic object recognition using a multifingered dextrous hand. In *Proceedings of the IEEE International Conference on Robotics and Automation*, pages 342–347, Scottsdale, AZ, May 1989. IEEE.

[2] M. Blauer and P.R. Belanger. State and parameter estimation for robotic manipulators using force measurements. *IEEE Transactions on Automatic Control*, 32(12):1055–1066, 1987.

[3] P. Dario and G. Buttazzo. An anthropomorphic robot finger for investigating artificial tactile perception. *International Journal of Robotics Research*, 6(3):25–48, 1987.

[4] R.E. Ellis. Planning tactile recognition paths in two and three dimensions. *International Journal of Robotics Research*, 11(2):87–111, 1992.

[5] A. Gelb, editor. *Applied Optimal Estimation.* M.I.T. Press, Cambridge, MA, 1974.

[6] S.J. Gordon and W.T. Townsend. Integration of tactile-force and joint-torque information in a whole-arm manipulator. In *Proceedings of the IEEE International Conference on Robotics and Automation*, pages 464–469, Scottsdale, AZ, May 1989. IEEE.

[7] R.A. Grupen. Planning grasp strategies for multifingered robot hands. In *Proceedings of the IEEE International Conference on Robotics and Automation*, pages 646–651, Sacramento, CA, April 1991. IEEE.

[8] R.A. Grupen, T.C. Henderson, and I.D. McCammon. A survey of general purpose manipulation. *International Journal of Robotics Research*, 8(1):38–62, 1989.

[9] M. Kaneko, H. Maekawa, and K. Tanie. Active tactile sensing by robotic fingers based on minimum-external-sensor-realization. In *Proceedings of the IEEE International Conference on Robotics and Automation*, pages 1289–1294, Nice, France, May 1992. IEEE.

[10] M. Kaneko and K. Tanie. Contact point detection for grasping of an unknown object using self-posture changeability (spc). In *Proceedings of the IEEE International Conference on Robotics and Automation*, pages 864–869, Cincinnati, OH, May 1990. IEEE.

[11] S. Narasimhan. Dextrous robotic hands: Kinematics and control. Technical Report AI TR 1056, Massachusetts Institute of Technology, 1988.

[12] H.R. Nicholls and M.H. Lee. A survey of robot tactile sensing technology. *International Journal of Robotics Research*, 8(3):3–30, 1989.

[13] J.R. Phillips, R.S. Johansson, and K.O. Johnson. Responses of human mechanoreceptive afferents to embossed dot arrays scanned across fingerpad skin. *Journal of Neuroscience*, 12(3):827–839, 1992.

[14] F. Reuleaux. *The Kinematics of Machinery.* reprinted by Dover Publications, INC., New York, NY, 1963. Translated and Edited by A.B.W. Kennedy in 1876.

[15] J.K. Salisbury. Interpretation of contact geometries from force measurements. In *Robotics Research: The First International Symposium*, pages 565–577. MIT Press, 1984.

[16] S.A. Stansfield. A haptic system for a multifingered hand. In *Proceedings of the IEEE International Conference on Robotics and Automation*, pages 658–664, Sacramento, CA, April 1991. IEEE.

[17] D.A. Sugden. Role of proprioception in eye-hand coordination. In *Development of Eye-Hand Coordination Across the Life Span*, pages 133–153. University of South Carolina Press, 1990.

[18] T. Tsujimura and T. Yabuta. A tactile sensing method employing force/torque information through insensitive probes. In *Proceedings of the IEEE International Conference on Robotics and Automation*, pages 1315–1320, Nice, France, May 1992. IEEE.

Manfred Huber received his "Vordiplom" from the University of Karlsruhe, Germany in 1990 and a M.S. in Computer Science from the University of Massachusetts at Amherst in 1993. He has been a research assistant with the Laboratory for Perceptual Robotics in this department since 1992. His research interests are in robotics and learning.

Roderic A. Grupen received a B.A. in Physics from Franklin and Marshall College and a B.S. in Mechanical Engineering from Washington University in 1980. His M.S. degree was granted by the Pennsylvania State University in 1984, and he received a Ph.D. in Computer Science from the University of Utah in 1988. Professor Grupen joined the Computer Science Department as an Assistant Professor in 1988 where he is a Co-Director of the CS Laboratory for Perceptual Robotics. This lab is concerned with sensor-based modeling and control, geometric reasoning, dextrous robotics, and the dynamic specification of resources and architectures for real-time autonomous systems.